Heavy hydrides: H$_2$Te ultraviolet photochemistry

J. Underwood, D. Chastaing, S. Lee, and C. Wittig[a)]
Department of Chemistry, University of Southern California, Los Angeles, California 90089

The room-temperature ultraviolet absorption spectrum of H$_2$Te has been recorded. Unlike other group-6 hydrides, it displays a long-wavelength tail that extends to 400 nm. Dissociation dynamics have been examined at photolysis wavelengths of 266 nm (which lies in the main absorption feature) and 355 nm (which lies in the long-wavelength tail) by using high-n Rydberg time-of-flight spectroscopy to obtain center-of-mass translational energy distributions for the channels that yield H atoms. Photodissociation at 355 nm yields TeH($^2\Pi_{1/2}$) selectively relative to the TeH($^2\Pi_{3/2}$) ground state. This is attributed to the role of the $3A'$ state, which has a shallow well at large $R_{\text{H-TeH}}$ and correlates to H+TeH($^2\Pi_{1/2}$). Note that the $^2\Pi_{1/2}$ state is analogous to the $^2P_{1/2}$ spin-orbit excited state of atomic iodine, which is isoelectronic with TeH. The $3A'$ state is crossed at large R only by $2A''$, with which it does not interact. The character of $3A'$ at large R is influenced by a strong spin-orbit interaction in the TeH product. Namely, $^2\Pi_{1/2}$ has a higher degree of spherical symmetry than does $^2\Pi_{3/2}$ (recall that I($^2P_{1/2}$) is spherically symmetric), and consequently $^2\Pi_{1/2}$ is not inclined to form either strongly bonding or antibonding orbitals with the H atom. The $3A' \leftarrow X$ transition dipole moment dominates in the long-wavelength region and increases with R. Structure observed in the absorption spectrum in the 380–400 nm region is attributed to vibrations on $3A'$. The main absorption feature that is peaked at $\sim$240 nm might arise from several excited surfaces. On the basis of the high degree of laboratory system spatial anisotropy of the fragments from 266 nm photolysis, as well as high-level theoretical studies, the main contribution is believed to be due to the $4A''$ surface. The $4A'' \leftarrow X$ transition dipole moment dominates in the Franck-Condon region, and its polarization is in accord with the experimental observations. An extensive secondary photolysis (i.e., of nascent TeH) is observed at 266 and 355 nm, and the corresponding spectral features are assigned. Analyses of the c.m. translational energy distributions yield bond dissociation energies D_0. For H$_2$Te and TeH, these are 65.0±0.1 and 63.8±0.4 kcal/mol, respectively, in good agreement with predictions that use high-level relativistic theory. © *2005 American Institute of Physics.* [DOI: 10.1063/1.2008261]

I. INTRODUCTION

Relativistic effects in chemistry are due mainly to the increased effective mass of electrons when they are in the vicinity of highly charged nuclei, and therefore have large velocities. In systems composed of light atoms, the approximation that the speed of light c is equal to infinity holds, whereas for systems that contain heavy atoms, this assumption breaks down and relativistic effects can be manifest in the photodissociation dynamics.

The core $1s$ electrons of a heavy atom travel at a significant percentage of the speed of light, and the corresponding increased effective mass of the electron leads to a significant contraction of the $1s$ orbital. Even though valence orbitals are affected to a lesser degree, the increased masses of the core electrons result in ionization potentials, oxidation states, and bond energies that would not be predicted by extrapolation from lighter counterparts.[1] Spin-orbit coupling also increases with the mass of the atom. When this coupling is large, spin and orbital angular momentum cease to have good quantum numbers. Singlet-triplet selection rules are no longer valid, and the terms "singlet" and "triplet" cease to be good descriptors. Consequently, "singlet-triplet" transitions can be quite strong and may even dominate in some regions of the spectra.

The photodissociation of systems containing heavy atoms has received modest attention relative to lighter counterparts. Many heavy atoms are toxic and their compounds are often unstable, necessitating collaborations with chemists who make molecules for a living. Theoretical studies are also demanding. The large number of electrons and the need to treat relativistic effects rigorously make such calculations difficult.[1–3]

One of the few systems in which theory and photodissociation experiments have explored relativistic effects thoroughly and with excellent agreement is the low-energy absorption spectrum of HI, i.e., 190-315 nm.[3] The absorption of a photon in this region leads to two product channels:

$$\text{HI} \rightarrow \text{H} + \text{I}(^2P_{3/2}), \tag{1}$$

$$\rightarrow \text{H} + \text{I}(^2P_{1/2}). \tag{2}$$

Reaction (1) yields ground state I($^2P_{3/2}$), while reaction (2) yields spin-orbit excited state I($^2P_{1/2}$); these states are separated by 7603 cm^{-1}.[4] Three excited states, $A\,^1\Pi_1$, $a\,^3\Pi_1$,
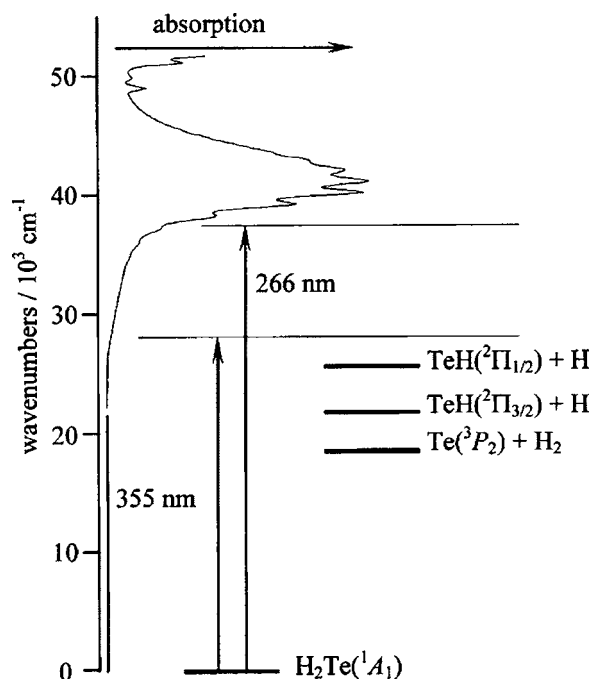
[a)]Electronic mail: wittig@usc.edu

FIG. 1. H_2Te absorption spectrum and possible product energies. Arrows indicate the photolysis wavelengths used in this study, 266 and 355 nm. The spectrum and product energies are determined in this study.

and $^3\Pi_{0+}$, are involved in the ultraviolet absorption and resulting dissociation that takes place throughout the HI low-energy absorption spectrum, which is usually referred to as the $A \leftarrow X$ band.

Recent calculations by Alekseyev *et al.* have increased our understanding of photodissociation in the HI $A \leftarrow X$ band and have guided our understanding of other heavy-atom systems.[2] They calculated the potential curves and transition dipole moments, including relativistic effects and spin-orbit coupling, and their results are in agreement with the numerous experimental data that have been acquired with HI.[5–14] Dissociation on $^1\Pi_1$ and $^3\Pi_1$ lead to $H+I(^2P_{3/2})$, whereas dissociation on $^3\Pi_{0+}$ leads to spin-orbit excited state $I(^2P_{1/2})$, hereafter referred to as I^*. Whereas the $^1\Pi_1$ and $^3\Pi_1$ states are repulsive, $^3\Pi_{0+}$ is weakly bound, i.e., by ~ 600 cm^{-1}. The minimum at ~ 2.7 Å is shifted significantly from the ground-state minimum of 1.6 Å, and calculations suggest that $^3\Pi_{0+}$ can support two vibrational levels. At small values of R, the absorption spectrum is dominated by the $^1\Pi_1 \leftarrow X$ and $^3\Pi_1 \leftarrow X$ transitions. At larger R, i.e., beginning around 1.9 Å, the $^3\Pi_{0+} \leftarrow X$ transition dominates.

Another model system for studying relativistic effects — and the subject of the study described herein — is H_2Te. It is isoelectronic with HI, and the lighter group-6 dihydrides (H_2O, H_2S, and H_2Se) have been studied in varying degrees of detail, providing bases for comparisons.[15–28] Three product channels are energetically accessible via the low-energy absorption band, as indicated in Fig. 1.[29]

$$H_2Te \rightarrow H_2 + Te, \tag{3}$$

$$\rightarrow H + TeH(^2\Pi_{3/2}, v, J), \tag{4}$$

$$\rightarrow H + TeH(^2\Pi_{1/2}, v, J), \tag{5}$$

where v and J are vibrational and rotational quantum numbers, respectively. Spin-orbit excited $TeH(^2\Pi_{1/2})$ lies 3815 cm^{-1} above ground state $TeH(^2\Pi_{3/2})$.[30] The photodissociation experiments presented in this study are sensitive only to reactions (4) and (5); the role of reaction (3) in the gas-phase photochemistry of the low-energy absorption features of H_2Te is unknown.

There have been only a few studies of the low-energy ultraviolet absorption features of H_2Te. In 1931, Goodeve and Stein carried out one of the earliest experiments, measuring the lowest-energy absorption bands of H_2O, H_2S, H_2Se, and H_2Te.[31] Though the spectra were taken at low resolution and there were contamination issues with the heavier group-6 dihydride samples, the H_2Te spectrum exhibited a strikingly different shape compared with those of the lighter dihydrides in the long-wavelength region. The absorption spectra of the lighter dihydrides drop off quickly toward longer wavelengths, and the spectra have similar shapes throughout their first absorption bands. On the other hand, rather than a sharp drop-off, H_2Te has a long tail that extends to ~ 400 nm. More recent studies have confirmed the absorption spectra of H_2O[16] and H_2S,[32] and we have measured the absorption of H_2Te, as shown in Fig. 1.[33] At the long-wavelength end of the absorption spectrum, though H_2S does not drop off as sharply as does H_2O, it does not exhibit the long structured tail that is seen in H_2Te.

In a preliminary report, we proposed that the structured long-wavelength tail in the absorption spectrum, as well as a propensity favoring reaction (5) over reaction (4), are consequences of a potential-energy surface (PES) that is bound weakly in the H–TeH coordinate.[33] This state correlates to the spin-orbit excited $TeH(^2\Pi_{1/2})$ product. It is similar to the $^3\Pi_{0+}$ state in isoelectronic HI, which correlates to $I(^2P_{1/2})$. The long-wavelength tail is intriguing, and it has been shown that it is of a relativistic origin,[3,33] namely, it is due to a strong spin-orbit interaction in the TeH product.

Prior to the acquisition of the experimental results that are presented below, only one theoretical study had been carried out on the low-lying electronic states of H_2Te. Sumathi and Balasubramanian calculated the geometries, bond energies, and ionization potentials of some of the low-lying states of H_2Te.[34] They predicted a H–TeH bond dissociation energy of $D_0 = 65 \pm 3$ kcal/mol ($22\,730 \pm 1050$ cm^{-1}). This is in good agreement with the experimental value we determined, 65.0 ± 0.1 kcal/mol ($22\,740 \pm 30$ cm^{-1}), as reported earlier.[33] Recently, Alekseyev *et al.* have calculated, at a high level of theory, the PES's of a number of low-lying electronic states and the corresponding transition dipole moments connecting the excited states and the ground state along the H–TeH coordinate.[3] They predicted $D_0 = 62$ kcal/mol ($21\,640$ cm^{-1}), which agrees with the experimental results to within the uncertainty of the calculations.

The experimental results presented below include significant contributions from secondary photolysis of TeH that derives from reactions (4) and (5). Namely, following photolysis of H_2Te, nascent internally excited TeH can absorb a photon and dissociate:
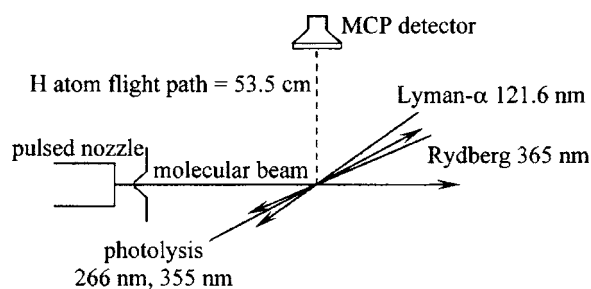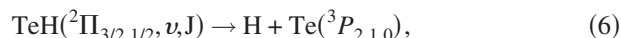
FIG. 2. Schematic of the high-n Rydberg time-of-flight (HRTOF) experimental arrangement. Polarized photolysis radiations (266 and 355 nm) and the radiations used to generate high-n Rydberg H atoms (121.6 and 365 nm) are indicated. The flight distance is 53.5 cm.

$$\text{TeH}(^2\Pi_{3/2,1/2}, v, \text{J}) \rightarrow \text{H} + \text{Te}(^3P_{2,1,0}), \qquad (6)$$

$$\rightarrow \text{H} + \text{Te}(^1D_2). \qquad (7)$$

Setzer *et al.* have calculated the low-lying electronic states of TeH and the corresponding transition dipole moments. They have predicted $D_e = 64$ kcal/mol (22 380 cm^{-1}),[35] while Balasubramanian *et al.* have predicted $D_e = 63 - 69$ kcal/mol (22 030 − 24 130 cm^{-1}).[36] Analyses of the secondary photolysis products in the results presented below indicate that D_0 for TeH is 63.8 ± 0.4 kcal/mol (22 300 ± 150 cm^{-1}).

II. EXPERIMENT

The H$_2$Te synthesis and the high-n Rydberg time-of-flight (HRTOF) arrangement have been described previously,[33,37] and therefore only a brief summary is given here. H$_2$Te is sensitive to temperature and light, necessitating a synthesis immediately prior to the HRTOF experiments. Samples were prepared by dripping HCl onto a ZnTe powder and collecting and purifying the resulting gas.[38] Care was taken to ensure that samples were not exposed to light during the synthesis and HRTOF experiments.

The room-temperature absorption spectrum of H$_2$Te was obtained by filling a cell with samples and recording the spectrum with a spectrophotometer (Varian Cary Series 50, resolution <1.5 nm). The cell was 9.5 cm long and it was fitted with MgF$_2$ windows. Structure in the long-wavelength tail was measured with a higher concentration by taking the spectrum immediately following synthesis (thus avoiding sample degradation) or by simply filling the cell with more samples.

For the HRTOF experiments indicated in Fig. 2, H$_2$Te diluted in an argon carrier was expanded to generate the molecular beam (General Valve, 0.8-mm orifice). The exact percentage of H$_2$Te in the beam is unknown, but by using different expansion conditions it was determined that contributions to the observed signals from clusters were minimal. Possible contributions of clusters to the observed signal are discussed below. Following expansion, the cold beam (several Kelvin) was collimated by a 1-mm-diameter skimmer 1 cm downstream from the nozzle. At the interaction region 5 cm downstream from the skimmer, linearly polarized radiation (355 or 266 nm) photolyzed the sample. The polarization was rotated with a $\lambda/2$ plate. The time delay of the
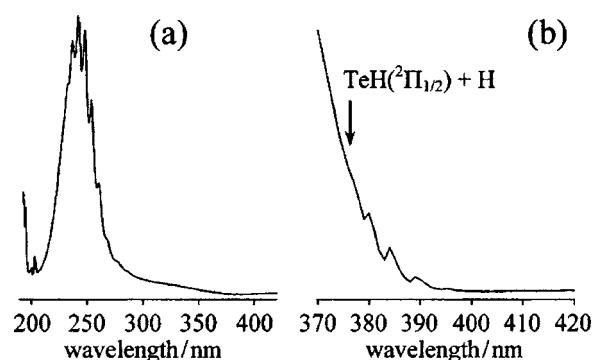

FIG. 3. (a) Absorption spectrum of H$_2$Te taken with a Varian Cary Series 50 spectrophotometer, resolution <1.5 nm. (b) A higher concentration sample emphasizes the long wavelength structure that corresponds to a vibrational frequency of ∼330 cm^{-1}.

photolysis radiation relative to the opening of the valve was adjusted such that the photolysis radiation intercepted the early part of the expansion, where clustering is minimal.

Nascent H atoms were probed via HRTOF spectroscopy. Radiation at 121.6 nm excited the H atom $2p \leftarrow 1s$ transition, followed by a radiation at ∼365 nm that excited a transition terminating on a high Rydberg level, i.e., $n \leftarrow 2p$, where n was typically ∼50. A weak dc field in the interaction region served two purposes. It repelled positive ions and it eliminated the $\Delta l = \pm 1$ angular momentum photoexcitation selection rule by making space anisotropic for the weakly bound high-n levels.[39] After traveling 53.5 cm, the Rydberg atoms were field ionized and detected with microchannel plates (MCP) arranged in a chevron configuration. The resulting time-of-flight spectra were transformed to center-of-mass (c.m.) translational energy spectra.

III. RESULTS

A. Absorption spectrum

The H$_2$Te absorption spectrum is shown in Fig. 3. Figure 3(b) emphasizes the structured long-wavelength tail, and the arrow indicates the energetic limit of the H+TeH($^2\Pi_{1/2}$) channel. The four peaks in the long-wavelength tail occur at 395.0, 389.0, 384.0, and 380.0 nm. The long-wavelength structure occurs below the energetic threshold for spin-orbit excited state TeH($^2\Pi_{1/2}$).

B. Photodissociation

The absorption spectrum of H$_2$Te and the relevant primary photolysis channels are shown in Fig. 1. HRTOF experiments were performed at two photolysis wavelengths in the first absorption band, 266 and 355 nm. Representative c.m. translational energy spectra are shown in Fig. 4. All of the data have been transformed from time-of-flight to c.m. translational energy with the assumption that the cofragments are TeH and H. Accounting for TeH+$h\nu \rightarrow$ Te+H leads to very minor corrections because of the large Te mass. Both primary and secondary photolysis events occur. For example, the 355 nm spectra exhibit peaks due to the following processes:
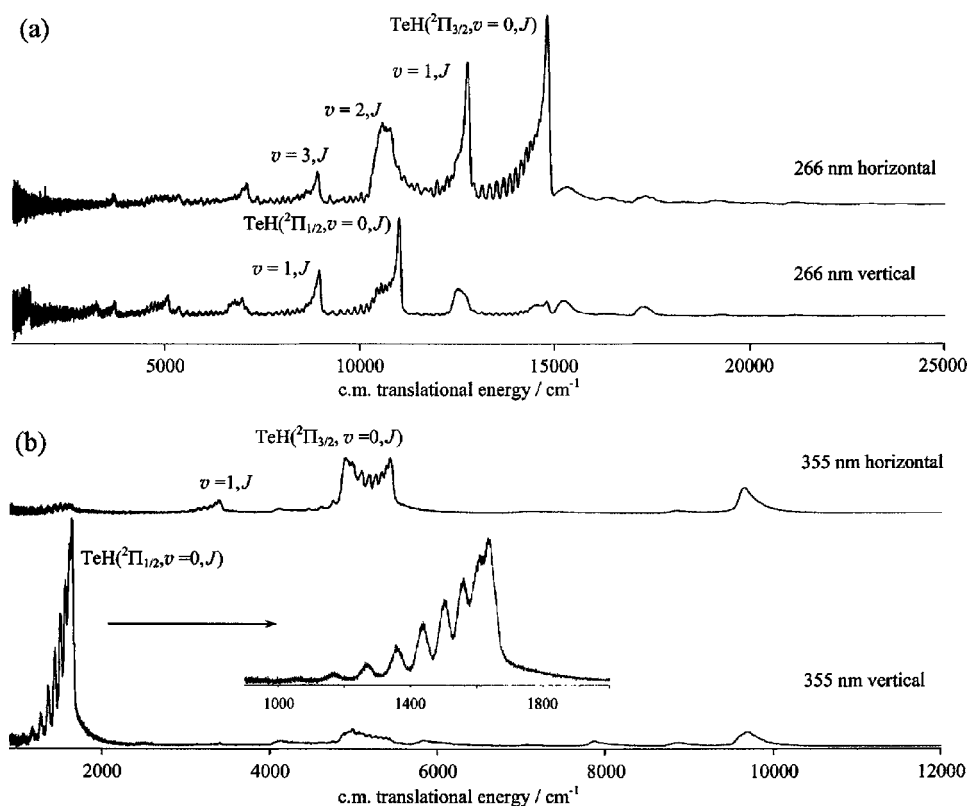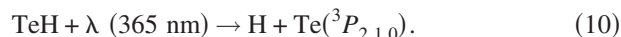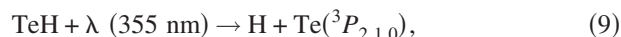
$$\text{H}_2\text{Te} + \lambda \ (355 \ \text{nm}) \rightarrow \text{H} + \text{TeH}(^2\Pi_{1/2,3/2}, v, J), \qquad (8)$$

FIG. 4. Center-of-mass translational energy distributions obtained with photolysis radiation at (a) 266 nm and (b) 355 nm. H$_2$Te is seeded in argon. The distributions shown in (a) were obtained by summing 1000 TOF spectra (one for each laser firing), and then transforming from time to energy. Likewise, the distributions shown in (b) were obtained by summing 2000 TOF spectra. Labels indicate some TeH internal states.

$$\text{TeH} + \lambda \ (355 \text{ nm}) \rightarrow \text{H} + \text{Te}(^3P_{2,1,0}), \qquad (9)$$

$$\text{TeH} + \lambda \ (365 \text{ nm}) \rightarrow \text{H} + \text{Te}(^3P_{2,1,0}). \qquad (10)$$

Reaction (8) is a primary photolysis process, while reactions (9) and (10) are secondary photolysis processes. The radiation for reaction (10) can come from the residual radiation from 121.6 nm generation (364.8 nm) and/or the Rydberg probe radiation (approximately 365 nm). The peaks with a resolved rovibrational structure result from primary photolysis events. Some of these are labeled with TeH quantum states in Fig. 4. The lumpy peaks are due to secondary photolysis processes; additional secondary photolysis peaks underlie the primary photolysis spectra and result in unusual peak structures. For example, a secondary photolysis peak lies at ~10 500 cm^{-1} in Fig. 4(a) and overlaps with primary photolysis peaks.

Results from primary photolysis processes will be presented first. The rationale for the assignment of the remaining features as secondary photolysis events, rather than dissociation of clusters or other events, will follow.

C. Primary photolysis: H$_2$Te→H+TeH

Results obtained by using photolysis with polarized 266 nm radiation are shown in Fig. 4(a). Unless otherwise noted, all of the data presented here have been obtained by expanding H$_2$Te in an argon carrier. The fragments are scattered with a high degree of anisotropy in the laboratory system. The major channel is TeH($^2\Pi_{3/2}$)+H, which is analogous to

the case of the ultraviolet photolysis of H$_2$Se.[28] Hydrogen atoms from the primary channel, TeH($^2\Pi_{3/2}$)+H, are detected with maximum selectivity when the 266 nm is horizontally polarized. On the other hand, vertical polarization results in selectivity toward the detection of the spin-orbit excited channel TeH($^2\Pi_{1/2}$)+H.

The production of TeH($^2\Pi_{1/2}$) results from a transition dipole moment that lies in the plane of H$_2$Te, whereas TeH($^2\Pi_{3/2}$) results from a transition dipole moment that is perpendicular to the H$_2$Te plane. The spin-orbit splitting measured in this study is in agreement with previous measurements,[30] and all of the rovibrational features have been assigned.

Photolysis with polarized 355 nm radiation yields a significantly different result than at shorter wavelengths, as shown in Fig. 4(b). As was the case with photolysis at 266 nm, the fragments are scattered with a high degree of anisotropy in the laboratory system. In contrast to the case of 266 nm photolysis, however, the excited spin-orbit state TeH($^2\Pi_{1/2}$) is populated preferentially. Of the H atoms that reach the detector, ~90% are due to TeH($^2\Pi_{1/2}$), corresponding to ~65% of the TeH product being formed in the $^2\Pi_{1/2}$ state.

Assignment of the primary photolysis peaks enables D_0 for H–TeH to be determined. The experimental value is 65.0±0.1 kcal/mol (22 740±30 cm^{-1}). This is in good agreement with theoretical predictions of 65±3 kcal/mol (22 730±1050 cm^{-1})[34] and 62 kcal/mol (21 640 cm^{-1}).[3]
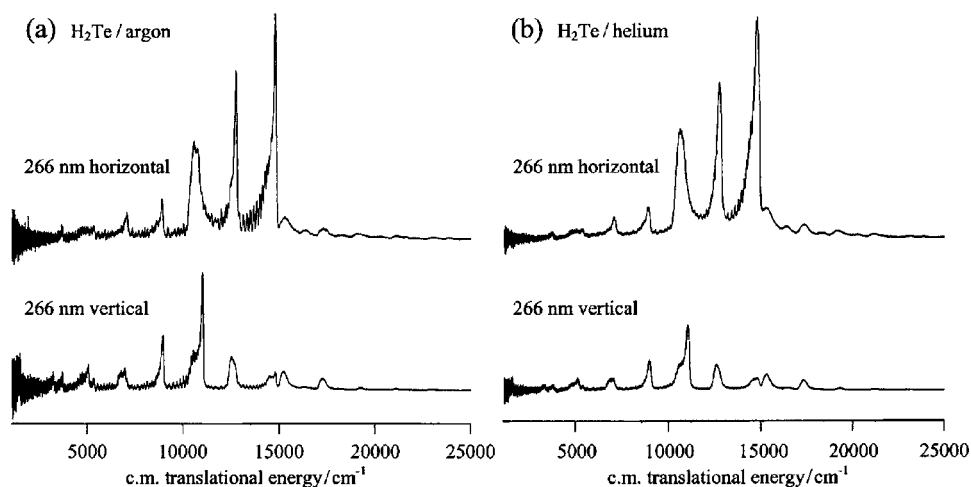
FIG. 5. Center-of-mass translational energy distributions for H$_2$Te seeded in (a) argon and (b) helium. Each spectrum represents 1000 shots per point, and the 266 nm photolysis radiation is polarized. Note that there is little, if any, discernible change in the lumpy features.

D. Secondary photolysis: TeH→H+Te

Though attempts were made to minimize contributions from so-called lumpy peaks in the spectra, it was not possible to eliminate these features, as can be seen in Fig. 4. They contribute significantly to the observed signals, even with low photolysis laser energies and under expansion conditions that are the least favorable for cluster formation. Similar effects have been observed in studies of H$_2$Se photodissociation.[28] Evidence is presented below that indicates that the lumpy features are due to secondary photolysis of the type indicated in Eqs. (9) and (10). They are not, to any significant extent, due to photodissociation of clustered species.

It has not been possible to determine the concentration of H$_2$Te that is seeded in the argon carrier to form the molecular beam. H$_2$Te is unstable and dissociates even at low temperatures and without exposure to light. The sample degrades over time on the metal surfaces of the foreline and the pulsed valve, despite the fact that the foreline has been shortened as much as possible. Because H$_2$Te decomposition produces H$_2$, the pressure in the sample reservoir cannot be used to estimate the H$_2$Te concentration.

Though the H$_2$Te concentration in the expansion is not known, a number of other factors have aided in the assignment of the lumpy peaks to secondary photolysis. Specifically, the conclusion that the lumpy features are due to secondary photolysis is supported by (i) changing the expansion conditions to alternately promote and discourage clustering, (ii) the assignment of each and every lumpy peak in the HRTOF spectra, and (iii) the dependence of the lumpy peaks on laser energy.

Referring to item (i), the lumpy features should depend markedly on seeding conditions if they are due to the photodissociation of clusters.[40] Figure 5 shows c.m. translational energy spectra obtained with 266 nm photolysis radiation using argon and helium alternately as carrier gases. The spectra were taken under otherwise identical experimental conditions and with approximately the same percentage of

H$_2$Te in the samples. No significant change was observed in the lumpy peaks. Thus, we conclude that clusters play a minimal role.

Referring to item (ii), Fig. 6 shows assignments of the lumpy peaks that are present when using 355 nm as the primary photolysis radiation. Secondary photolysis is considered for both 355 nm and what we refer to as 365 nm. The latter is present in the interaction region as either or both of the separate wavelengths that are used to (a) generate Lyman-α (i.e., 364.8 nm) and (b) promote the resulting excited H atoms from $n=2$ to a high-n Rydberg level (i.e., approximately 365 nm). Taken together, we refer to these radiations as 365 nm.

The vertical grids in Fig. 6 for 355 and 365 nm are displaced horizontally from one another by the difference in the photon energies, i.e., 770 cm^{-1}. Entries are included for 355 nm; it is understood that they are the same for 365 nm, but displaced to lower energy by 770 cm^{-1}. For example, the peak on the far right is assigned to the 355 nm photodissociation of TeH($^2\Pi_{1/2}, v=0, J$), yielding H+Te($^3P_2$), and the peak to its immediate left is assigned to the 365 nm photodissociation of TeH($^2\Pi_{1/2}, v=0, J$), yielding H+Te($^3P_2$). Note that the atomic tellurium $^3P_1$ and $^3P_0$ states are separated by only 44 cm^{-1}, so they are not resolved. These states taken together are designated as $^3P_{1,0}$. Thus, the spectrum shown in Fig. 6 is rationalized to within the accuracy of the measurements on the basis of secondary photolysis.

The above assignments yield a TeH dissociation energy of $D_0=63.8\pm0.4$ kcal/mol (22 300 cm$^{-1}\pm150$ cm^{-1}). This value is in agreement with the two calculations of D_e that have been carried out. Namely, Setzer et al. have predicted D_e of 64 kcal/mol,[35] while Balasubramanian et al. have predicted D_e of 63–69 kcal/mol.[36] By using the experimental value of 2054 cm^{-1} for the energy of the $v=1$ level,[41] our D_0 value yields $D_e=66.7\pm0.4$ kcal/mol (23 330 cm$^{-1}\pm150$ cm^{-1}).

The assignment of the 355 nm secondary photolysis peaks was relatively straightforward because a modest number of TeH states are populated via the primary photolysis event and limited secondary photolysis channels are acces-
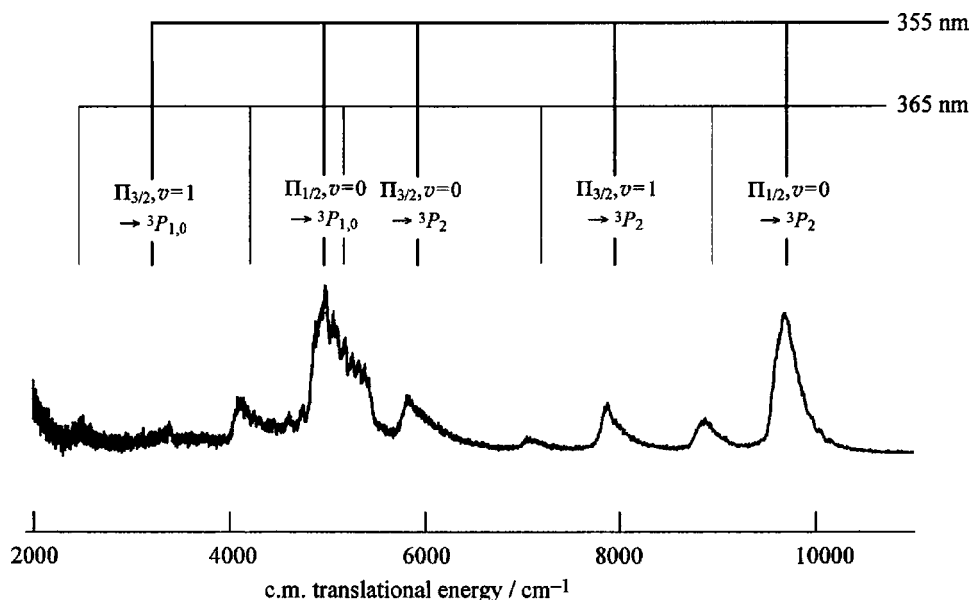
FIG. 6. The spectrum is from Fig. 4(b) (vertical polarization). The 355 nm photolysis of TeH can yield peaks at the approximate positions of the vertical lines. The entry labeled $^2\Pi_{1/2}$, $v=0 \rightarrow {}^3P_2$ denotes the Te($^3P_2$)+H channel from the 355 nm photodissociation of TeH($^2\Pi_{1/2}$, $v=0,J$). There are no entries listed for 365 nm. They are the same as for 355 nm, but shifted to lower energy by 770 cm^{-1}.

sible (see Fig. 7). On the other hand, at 266 nm, more channels are energetically accessible for both primary and secondary processes (see Fig. 8). Nevertheless, the assignment of the secondary photolysis peaks that are observed when photolyzing at 266 nm was accomplished in a similar manner as for the 355 nm case above. There were no surprises, and all of the lumpy features were reconciled by invoking secondary photolysis. Moreover, it was found that secondary photolysis was achieved exclusively by 266 nm radiation, rather than with contributions from 365 nm.

The D_0 value of 63.8±0.4 kcal/mol (22 330 cm^{-1} ±150 cm^{-1}) obtained from the 355 data fits the 266 nm data

as well. This D_0 value is the main result of the analyses of secondary photolysis processes. The nascent population distributions of the Te states that arise from TeH photodissociation, while interesting, are not of concern in the present study.

Finally, referring to item (iii), we consider how the lumpy peaks depend on laser energy. Because of sample degradation, it was not possible to obtain good quality data for peak height versus laser energy. Nevertheless, as discussed below, the dependencies on photolysis energy shown in Fig. 9 support the assignment presented in item (ii).

Translational energy distributions for 355 nm primary photolysis are shown in Figs. 9(a) and 9(b), which were re-
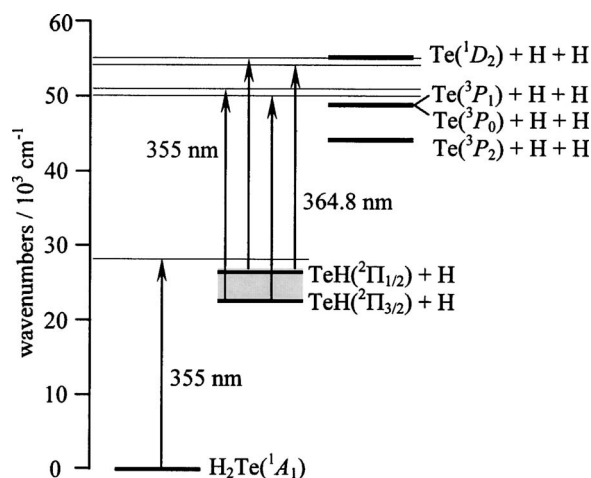

FIG. 7. Energy-level diagram of possible TeH secondary photolysis channels when 355 nm is the primary photolysis wavelength. Secondary photolysis of the nascent TeH product is observed for radiation at both 355 and 365 nm (i.e., residual radiation from the generation of the 121.6 nm and/or the Rydberg probe radiation). Shading indicates the internal energy range of products observed in both. The Te energy levels are from Ref. 4. The unusual ordering of the ^3P states is due to the strong spin-orbit coupling of $^3P_0$ with $^1S_0$ (Ref. 35). The $^1S_0$ state lies 18 492 cm^{-1} above $^3P_0$ (Ref. 4). Note that the $^3P_0$ and $^3P_1$ states are separated by 44 cm^{-1}.
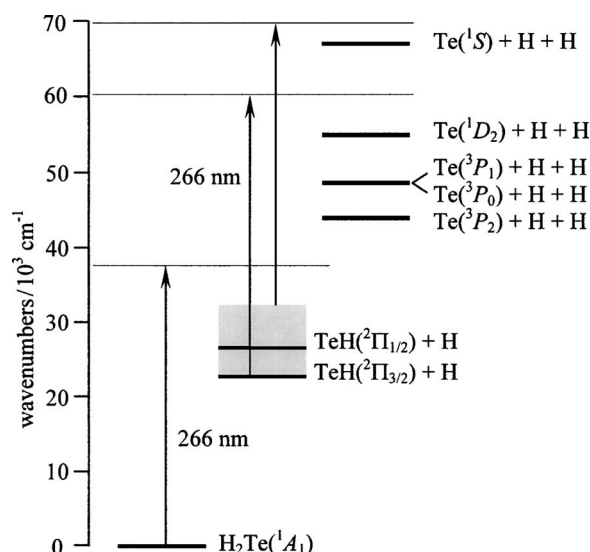

FIG. 8. Energy-level diagram of TeH secondary photolysis channels when 266 nm is the primary photolysis wavelength. Secondary photolysis of the TeH product is only observed for the 266 nm radiation. Shading indicates the internal energy range of products observed in the primary process.
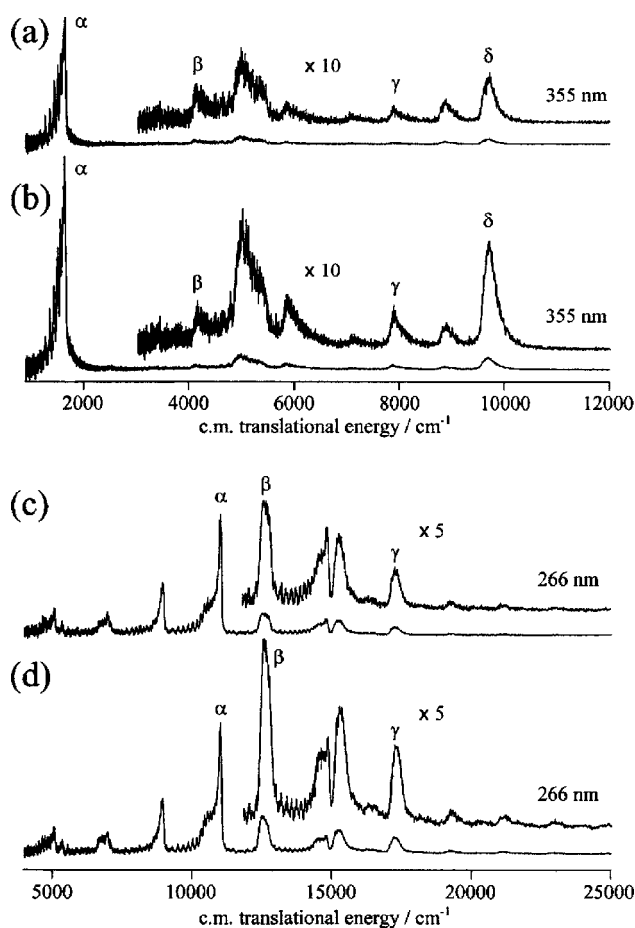
FIG. 9. Dependence of spectral features on photolysis energy. At 355 nm, c.m. translational energy distributions (100 shots per point) are given for laser energies, (a) 37 mJ and (b) 49 mJ. See text for details. The peaks labeled α are attributed to the H$_2$Te photolysis. Peaks labeled β are due to the secondary photolysis in which TeH absorbs a 365 nm photon. Peaks labeled γ and δ are attributed to the 355 nm secondary photolysis. At 266 nm, c.m. translational energy distributions (100 shots per point) are given for laser energies, (c) 26 mJ and (d) 49 mJ. Peaks labeled α are attributed to the H$_2$Te photolysis. Peaks labeled β and γ are attributed to the 355 nm secondary photolysis.

corded with 37 and 49 mJ, respectively. As mentioned above, because of sample instability, it is not possible to make a simple comparison of peak heights from one trace to the next. For example, the ratio of the laser energies (i.e., 49/37=1.3) is smaller than the ratio of the α peak heights for traces 9(b) and 9(a) (i.e., α_b/α_a=1.7), even though it is known that the α peaks are due to one-photon H$_2$Te photolysis. Were the samples stable, the two ratios would be the same or close.

It is possible, however, to normalize peak heights within a given trace to facilitate comparisons between traces. Relative intensities within a trace are accurate because entire TOF spectra are recorded with each laser firing. Let us take the ratios of the γ and δ peaks for Figs. 9(a) and 9(b), i.e., γ_b/γ_a and δ_b/δ_a. The ratio of the α peaks, α_b/α_a, is 1.7, and the α peaks are known to be due to one-photon photolysis. Were the ratios γ_b/γ_a and δ_b/δ_a due also to a one-photon process, they would have values of approximately 1.7. Instead, they are approximately equal to 2.8, which is close to 1.7^2. This is consistent with secondary photolysis.

Regarding the β peak, the signal does not increase significantly. As discussed above, it is assigned to secondary photolysis in which TeH($^2\Pi_{1/2}$, v=0) absorbs a 365 nm photon. The peak intensities of the unlabeled lumpy features shown in Figs. 9(a) and 9(b) are also consistent with the assignments shown in Fig. 6.

A similar analysis has been carried out for 266 nm primary photolysis; see Figs. 9(c) and 9(d), with respective energies of 26 and 49 mJ. Primary photolysis is nearly saturated (α_d/α_c=1.1) because the absorption coefficient is much larger at 266 nm than at 355 nm. Each of the ratios β_d/β_c and γ_d/γ_c is equal to approximately 1.9, which is close to the ratio of the photolysis energies (49/26=1.88). This is consistent with secondary photolysis in the case where the primary photolysis process is near saturation. There is no evidence for 365 nm secondary photolysis in Figs. 9(c) and 9(d).

IV. DISCUSSION

The experimental H atom translational energy distributions for the (primary) photolysis of H$_2$Te and the (secondary) photolysis of its nascent TeH product provide information about each of these species as well as the photoinitiated dynamical processes that they undergo. The fact that the H$_2$Te molecules have been expansion cooled, combined with the good HRTOF resolution of the primary photolysis products, yield detailed data concerning the photodissociation dynamics of this system. The large range of internal energies of the nascent TeH prohibits us from obtaining as much detailed information as in the case of H$_2$Te. Namely, TeH is produced with broad ranges of internal energies: up to ~3900 cm^{-1} for 355 nm photolysis and up to ~23 000 cm^{-1} for 266 nm photolysis. Nonetheless, conclusions can also be reached about the TeH system.

The assignment of the long-wavelength structure in the H$_2$Te absorption spectrum and a discussion of the photodissociation dynamics at 355 nm are presented first. The photochemistry in this region involves only a few low-lying electronic states. At shorter wavelengths, more electronic states are involved. Assignment of the absorption spectrum at the shorter wavelengths is less clear cut, but analysis of the 266 nm photodissociation results aids in determining the respective roles of the various electronic states in this region. Finally, a brief analysis of the secondary photolysis results is presented.

A. H$_2$Te

Alekseyev *et al.* have calculated the low-lying PES's in the H–TeH coordinate (see Fig. 10), as well as the corresponding transition dipole moments that connect these PES's to the ground state.[3] One of the most striking features is the weakly bound 3A' state. Its shape in the H–TeH coordinate is remarkably similar to that of the $^3\Pi_{0^+}$ curve in isoelectronic HI.[2] We proposed previously that there should exist a TeH state that is analogous to HI($^3\Pi_{0^+}$) in the H–TeH coordinate.[33]

The electron density of the highest energy orbital of the $^2\Pi_{1/2}$ excited spin-orbit state of TeH is smaller near the
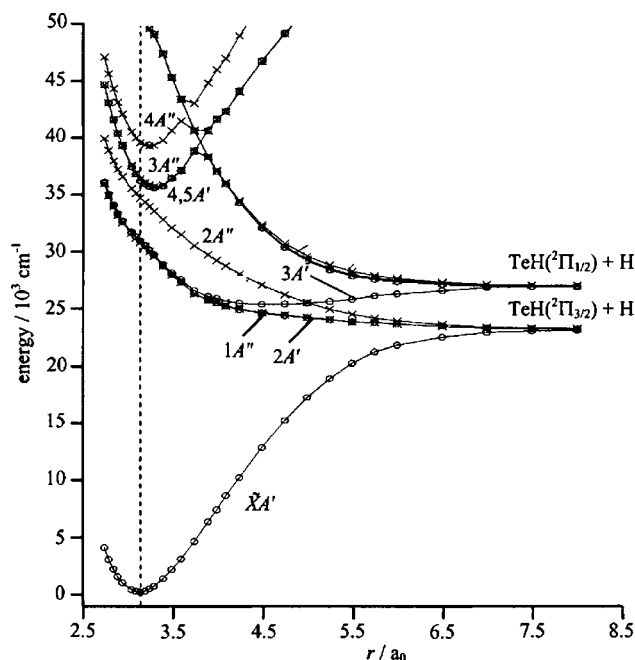
FIG. 10. H_2Te curves, from Ref. 3. The H_2Te bond angle and one TeH bond length are held at their ground equilibrium values of 90.3° and 1.67 Å.

nucleus compared with that of the $^2\Pi_{3/2}$ lower spin-orbit state, making the $^2\Pi_{1/2}$ state more spherical than the $^2\Pi_{3/2}$ state. Recall that the analogous atomic iodine spin-orbit state $^2P_{1/2}$ is spherically symmetric.[42] The significant TeH spin-orbit splitting of 3815 cm^{-1} acts to preserve these states in the large-R region of the H–TeH coordinate. Thus, TeH($^2\Pi_{1/2}$) is not inclined to form either strongly bonding or antibonding orbitals with the H atom. As in HI, this results in a shallow van der Waals well on the $3A'$ PES that correlates to spin-orbit excited TeH($^2\Pi_{1/2}$). The minimum of such a state lies at large R relative to the ground-state equilibrium geometry, i.e., respectively, 2.4 vs 1.67 Å in H_2Te, and 2.7 vs 1.6 Å in HI. Calculations along the H–TeH coordinate predict that the $3A'$ surface is bound by ~1620 cm^{-1}.[3] Preliminary calculations that include all degrees of freedom indicate that the binding energy is ~1780 cm^{-1}.[3]

We attribute the long-wavelength structure in the absorption spectrum shown in Fig. 3(b) to vibrations of H_2Te on the $3A'$ PES. The separation between the peaks corresponds to a frequency of ~330 cm^{-1}, and the structured part of the spectrum lies at energies that are below the energetic threshold for TeH($^2\Pi_{1/2}$). The widths of the features can, in principle, be due to several factors: (i) occupancy of rotational levels in the room-temperature sample, (ii) dissociation on the $3A'$ PES via a pathway that leads to H_2+Te, and (iii) coupling of $3A'$ to the $2A'$ PES.

Referring to item (i), the observed features have widths that are comparable to that of the band of transitions in which each originates from a different rotational level. An absorption or photofragment yield spectrum recorded with an expansion-cooled sample would eliminate this source of width.

Referring to item (ii), the H_2+Te channel is energetically accessible, and the possibility exists that dissociation via this channel occurs on the $3A'$ PES, in which case rapid

dissociation can yield a broad width. Only if dissociation is extremely rapid, however, can this mechanism alone reconcile the observed widths. This region of the PES has not been examined at a high level of theory, so this issue remains open. Referring to Fig. 10, though $3A'$ is crossed near its minimum energy by $2A''$, vibronic coupling between these surfaces is symmetry forbidden. Nonadiabatic coupling via Coriolis interaction can take place, but this will be too weak to reconcile the observed widths. Moreover, the 355 nm photolysis results indicate that coupling between $3A'$ and $2A''$ is negligible for rotationally cold molecules.

Referring to item (iii), it is possible for the $2A'$ PES to intersect, or come close to, the $3A'$ PES. This can be determined through an exploration of the full configuration space using a high level of theory. If such an intersection (or near-intersection) seam is found, it will play a prominent role in the dynamics when it lies at energies that are below those of the photoexcitation.

At 355 nm, ~65% of the H+TeH reaction products accrue via the spin-orbit excited H+TeH($^2\Pi_{1/2}$) product channel.[33] Such a propensity has been observed previously, following the broadband photolysis of H_2Te.[43] It is due to the participation of the $3A'$ state (see Fig. 10).

In the Franck–Condon region, the $3A' \leftarrow X$ and $2A' \leftarrow X$ transition dipole moments are modest, and it has been shown that both transitions are of primarily singlet to triplet character.[3] The $1A'' \leftarrow X$ transition dipole moment is an order of magnitude smaller than these, and therefore it is relatively unimportant and will not be considered further. The observed selectivity toward photodissociation via the spin-orbit excited product channel is due to the behavior of the $3A' \leftarrow X$ transition dipole moment outside the Franck–Condon region. Namely, it increases significantly with H–TeH distance because of the increasingly singlet character of $3A'$ with increasing R_{H-TeH}.[3]

In the wavelength range of 210–300 nm, a number of states might contribute to the absorption spectrum, as can be seen in Fig. 10. The $4A'' \leftarrow X$ transition dipole moment dominates in the Franck–Condon region. Though transition dipole moments connecting the ground state to $3A'$, $4A'$, $5A'$, and $3A''$ are all an order of magnitude smaller, they may play a role. Analysis of the 266 nm photolysis results can help to sort out the possible contributions to the absorption spectrum in the main part of the absorption band.

Photodissociation with horizontally polarized 266 nm radiation leads mainly to TeH($^2\Pi_{3/2}$). This channel arises from one or more transition dipole moments that lie perpendicular to the plane of the molecule. We assign this to $4A'' \leftarrow X$, as this is the strongest of such transitions. The fact that TeH($^2\Pi_{1/2}$) results mainly from one or more transition dipole moments that lie in the plane of the molecule indicates that this species does not arise from coupling of $4A''$ to a state that correlates to TeH($^2\Pi_{1/2}$). The $3A'$, $4A'$, and $3A''$ states correlate with the spin-orbit excited channel. However, because the transition dipole moment is in the plane of the molecule, $3A''$ is ruled out as a major participant. In the Franck–Condon region, $4A' \leftarrow X$ has the larger transition dipole moment, but $3A' \leftarrow X$ is also possible.

The main features of the lowest-energy absorption bands

of H_2O, H_2S, and H_2Te display structure that is superimposed on a broad background, with H_2Te and H_2S having narrower structures than H_2O.[16,32] An absorption spectrum of H_2Se at a sufficient resolution to discern such structure has not been published. Excitation in the main region of the first absorption band of H_2O involves only one excited electronic state, $\widetilde{A}\ ^1B_1$, and the structure has been assigned to a large-amplitude symmetric stretching motion on the mainly repulsive $\widetilde{A}\ ^1B_1$ state.[18] Two electronic states are involved in the lowest-energy H_2S absorption band. Excitation is primarily to the bound $^1B_1$ state, which is coupled via a nonadiabatic interaction to the dissociative $^1A_2$ state. Symmetric stretch motion on the bound state leads to the observed structure.[18,44]

As discussed above, the $4A'' \leftarrow X$ transition dominates the main part of the low-energy H_2Te absorption spectrum. The $4A''$ state is bound in the H–TeH coordinate, and structure at wavelengths less than ~260 nm can be attributed to Te–H stretch. The source of the widths is unclear. The $^3B_1$ state from which $4A''$ arises is repulsive in the $H_2 + Te$ coordinate when spin-orbit coupling is not included, and calculations in this coordinate including a spin-obit coupling have not yet been performed. Numerous other low-lying electronic states lie in the region of $4A''$, and coupling to one or more of these might contribute to the widths.

B. TeH

Broadband photolysis studies of H_2Te and TeH have identified spectral regions in which their ultraviolet absorptions coincide.[45] The results presented above indicate that this is also true at the relatively long wavelengths examined here. Setzer *et al.* have calculated the low-lying states of TeH, the majority of which are repulsive.[35] A number of these might participate at the energies accessed in this study, e.g., according to the multiple dissociation channels shown in Figs. 7 and 8. Interestingly, an $\Omega = 1/2$ state that correlates asymptotically with $Te(^2P_0) + H$ is believed to be weakly bound with a minimum at ~3 Å.[35] The significant internal excitation of the nascent TeH prior to its photolysis prohibits any determination of the respective roles of the $^2\Pi_{3/2}$ and $^2\Pi_{1/2}$ states in the dissociation dynamics.

V. CONCLUSIONS

Excitation of H_2Te in its lowest-energy absorption system involves a number of electronic states. In the main part of the band (210–300 nm), the $4A'' \leftarrow X$ transition dominates, while $3A'$, $4A'$, and $5A'$ probably contribute, but to a lesser degree.

In the long-wavelength tail, the $3A'$ state plays the most significant role. Though the $3A' \leftarrow X$ transition is weak in the Franck–Condon region, its transition dipole moment at large R is significantly stronger than those that connect the ground state to other excited surfaces. The $3A'$ state is crossed by $2A''$ near its minimum, but nothing much happens, as interaction can take place only via a Coriolis interaction. For example, the propensity toward $TeH(^2\Pi_{1/2})$ observed with 355 nm photolysis radiation and the resolved structure in the long-wavelength tail of the absorption spectrum suggest that

coupling between these states is small. The long-wavelength structure in the absorption spectrum (370–400 nm) is consistent with a weakly bound well at large R on the PES leading to spin-orbit excited state $TeH(^2\Pi_{1/2})$. The source of this bound character is relativistic in nature: decreasing the spin-orbit coupling decreases the bound character.

The HRTOF spectra yield bond dissociation energies. For H_2Te we have obtained $D_0 = 65.0 \pm 0.1$ kcal/mol, in agreement with theoretical predictions: 65 ± 3 kcal/mol (Ref. 34) and 62 kcal/mol.[3] For HTe, we have obtained $D_0 = 63.8 \pm 0.4$ kcal/mol. This is in agreement with theoretical predictions of D_e: 64 kcal/mol (Ref. 35) and 63–69 kcal/mol.[36] Namely, by using the experimental value of 2054 cm^{-1} for the energy of the $v = 1$ level,[41] our D_0 value yields $D_e = 66.7 \pm 0.4$ kcal/mol.

An interesting issue is whether weakly bound surfaces having minima at large R, such as $3A'$ in H_2Te, are common in molecules that contain heavy atoms. For example, weakly bound $HI(^3\Pi_{0+})$ can be accessed by photolyzing vibrationally excited HI, and indirect evidence of $HI(^3\Pi_{0+})$ has been observed in intracluster superelastic scattering of H from I^*.[46]

It is intriguing to consider the type of vibrational motion associated with the long-wavelength structure. Calculations on the $3A'$ surface indicate that it can support roughly five vibrational levels.[3]

The photochemistry of molecules that contain heavy atoms is rich. Large numbers of low-lying electronic states and the breakdown of singlet-triplet selection rules facilitates the participation of a number of electronic states at modest energies. Spin-orbit coupling affects shapes of potentials, resulting in unusual photochemistry, and intuition gained from studying lighter systems may not apply to molecules that contain heavy atoms.

[1] K. Balasubramanian, *Relativistic Effects in Chemistry* (Wiley, New York, 1997), Pts. A and B.
[2] A. B. Alekseyev, H.-P. Liebermann, D. B. Kokh, and R. J. Buenker, J. Chem. Phys. **113**, 6174 (2000).
[3] A. B. Alekseyev, H.-P. Liebermann, and C. Wittig, J. Chem. Phys. **121**, 9389 (2004).
[4] C. E. Moore, *Atomic Energy Levels* (National Bureau of Standards, Washington, D.C. 1971).
[5] P. Brewer, P. Das, G. Ondrey, and R. Bersohn, J. Chem. Phys. **79**, 720 (1983).
[6] R. D. Clear, S. J. Riley, and K. R. Wilson, J. Chem. Phys. **63**, 1340 (1975).
[7] D. J. Gendron and J. W. Hepburn, J. Chem. Phys. **109**, 7205 (1998).
[8] S. R. Langford, P. M. Regan, A. J. Orr-Ewing, and M. N. R. Ashfold, Chem. Phys. **231**, 245 (1998).
[9] J. F. Ogilvie, Trans. Faraday Soc. **67**, 2205 (1971).
[10] P. M. Regan, D. Ascenzi, C. Clementi, M. N. R. Ashfold, and A. J. Orr-Ewing, Chem. Phys. Lett. **315**, 187 (1999).
[11] R. Schmiedl, H. Dugen, W. Meier, and K. H. Welge, Z. Phys. A **304**, 137 (1982).

[12] G. N. A. van Veen, K. A. Mohamed, T. Baller, and A. E. de Vries, Chem. Phys. **80**, 113 (1983).

[13] C. A. Wight and S. R. Leone, J. Chem. Phys. **79**, 4823 (1983).

[14] Z. Xu, B. Koplitz, and C. Wittig, J. Phys. Chem. **92**, 5518 (1988).

[15] V. Engel, V. Staemmler, R. L. Vander Wa, F. F. Crim, R. J. Sension, B. Hudson, P. Anderson, S. Hennig, K. Weide, and R. Schinke, J. Phys. Chem. **96**, 3201 (1992).

[16] P. Gürtler, V. Saile, and E. E. Koch, Chem. Phys. Lett. **51**, 393 (1977).

[17] D. F. Plusquellic, O. Votava, and D. J. Nesbitt, J. Chem. Phys. **107**, 6123 (1997).

[18] R. Schinke, *Photodissociation Dynamics* (Cambridge University Press, Cambridge, 1993).

[19] T. Schröder, R. Schinke, M. Ehara, and K. Yamashita, J. Chem. Phys. **109**, 6641 (1998).

[20] M. N. R. Ashfold, Adv. Photochem. **21**, 217 (1996).

[21] D. C. Dobson, F. C. James, I. Safarik, H. E. Gunning, and O. P. Strausz, J. Phys. Chem. **79**, 771 (1975).

[22] S. T. Gibson, J. P. Greene, and J. Berkowitz, J. Chem. Phys. **85**, 4815 (1986).

[23] B. Lindgren, J. Mol. Spectrosc. **28**, 536 (1968).

[24] M. Pericou-Cayere, M. Gelize, and A. Dargelos, Chem. Phys. **214**, 1997 (1997).

[25] W. C. Price, J. P. Teegan, and A. D. Walsh, Proc. R. Soc. London, Ser. A **201**, 600 (1950).

[26] D. Simah, B. Hartke, and H.-J. Werner, J. Chem. Phys. **111**, 4523 (1999).

[27] J. E. Stevens, R. K. Chaudhuri, and K. F. Freed, J. Chem. Phys. **105**, 8754 (1996).

[28] X. Zhang, M. Johnson, K. T. Lorenz, K. A. Cowen, and B. Koplitz, J. Phys. Chem. A **104**, 10511 (2000).

[29] R. J. Donovan, D. J. Little, and J. Konstantatos, J. Photochem. **1**, 86 (1972).

[30] D. A. Gillett, J. P. Towle, M. Islam, and J. M. Brown, J. Mol. Spectrosc. **163**, 459 (1994).

[31] C. F. Goodeve and N. O. Stein, Trans. Faraday Soc. **27**, 393 (1931).

[32] C. Y. R. Wu and F. Z. Chen, J. Quant. Spectrosc. Radiat. Transf. **60**, 17 (1998).

[33] J. Underwood, D. Chastaing, S. Lee, P. Boothe, T. C. Flood, and C. Wittig, Chem. Phys. Lett. **362**, 483 (2002).

[34] K. Sumathi and K. Balasubramanian, J. Chem. Phys. **92**, 6604 (1990).

[35] K. D. Setzer, E. H. Fink, A. B. Alekseyev, H.-P. Liebermann, and R. J. Buenker, J. Mol. Spectrosc. **206**, 181 (2001).

[36] K. Balasubramanian, M. Han, and M. Z. Liao, J. Chem. Phys. **86**, 4979 (1987).

[37] J. Zhang, C. W. Riehn, M. Dulligan, and C. Wittig, J. Chem. Phys. **104**, 7027 (1996).

[38] L. M. Dennis and R. P. Anderson, J. Am. Chem. Soc. **36**, 882 (1914).

[39] T. F. Gallagher, *Rydberg Atoms* (Cambridge University Press, New York, 1994).

[40] *Atomic and Molecular Beam Methods*, edited by G. Scoles (Oxford University Press, New York, 1988), Vol. I.

[41] E. H. Fink and K. D. Setzer, J. Mol. Spectrosc. **138**, 19 (1989).

[42] R. N. Zare, *Angular Momentum* (Wiley, New York, 1988).

[43] D. J. Little, R. J. Donovan, and R. J. Butcher, J. Photochem. **2**, 451 (1973).

[44] D. Skouteris, B. Hartke, and H.-J. Werner, J. Phys. Chem. A **105**, 2458 (2001).

[45] R. J. Donovan, D. J. Little, and J. Konstantatos, J. Chem. Soc., Faraday Trans. 2 **68**, 1812 (1972).

[46] D. Chastaing, J. Underwood, and C. Wittig, J. Chem. Phys. **119**, 928 (2003).